



## Article

# The Performance of Commonly Used Surface-Based Instruments for Measuring Visibility, Cloud Ceiling, and Humidity at Cold Lake, Alberta

Faisal S. Boudala <sup>1,\*</sup>, Ismail Gultepe <sup>1</sup> and Jason A. Milbrandt <sup>2</sup>

<sup>1</sup> Meteorological Research Division, Environment and Climate Change Canada, Toronto, ON 66777, Canada; ismail.Gultepe@ec.gc.ca

<sup>2</sup> Meteorological Research Division, Environment and Climate Change Canada, Dorval, QC H9P 1J3, Canada; jason.Milbrandt@ec.gc.ca

\* Correspondence: faisal.bouda@ec.gc.ca

**Abstract:** Data from automated meteorological instruments are used for model validation and aviation applications, but their measurement accuracy has not been adequately tested. In this study, a number of ground-based in-situ, remote-sensing instruments that measure visibility (VIS), cloud base height (CBH), and relative humidity (RH) were tested against data obtained using standard reference instruments and human observations at Cold Lake Airport, Alberta, Canada. The instruments included the Vaisala FS11P and PWD22 (FSPW), a profiling microwave radiometer (MWR), the Jenoptik ceilometer, Rotronic, Vaisala WXT520, AES-Dewcell RH, and temperature sensors. The results showed that the VIS measured using the FSPWs were well correlated with a correlation coefficient (R) of 0.84 under precipitation conditions and 0.96 during non-precipitating conditions (NPC), indicating very good agreement. However, the FS11P on average measured higher VIS, particularly under NPC. When the FSPWs were compared against human observation, a significant quantization in the data was observed, but less was noted during daytime compared to nighttime. Both probes measured higher VIS compared to human observation, and the calculated R was close to 0.6 for both probes. When the FSPWs were compared against human observation for VIS < 4 km, the calculated mean difference (MD) for the PWD22 (MD ≈ 0.98 km) was better than the FS11P (MD ≈ 1.37 km); thus, the PWD22 was slightly closer to human observation than the FS11P. No significant difference was found between daytime and nighttime measured VIS as compared to human observation; the instruments measured slightly higher VIS. Two extinction parameterizations as functions of snowfall rate were developed based on the VFPs measurements, and the results were similar. The Jenoptik ceilometer generally measured lower CBH than human observation, but the MWR measured larger CBHs for values < 2 km, while CBHs were underestimated for higher CBHs.

**Keywords:** ceilometer and radiometric profiling; visibility; cloud base height; relative humidity



**Citation:** Boudala, F.S.; Gultepe, I.; Milbrandt, J.A. The Performance of Commonly Used Surface-Based Instruments for Measuring Visibility, Cloud Ceiling, and Humidity at Cold Lake, Alberta. *Remote Sens.* **2021**, *13*, 5058.

<https://doi.org/10.3390/rs13245058>

Academic Editors: Simone Lolli and Carmine Serio

Received: 17 October 2021

Accepted: 8 December 2021

Published: 13 December 2021

**Publisher's Note:** MDPI stays neutral with regard to jurisdictional claims in published maps and institutional affiliations.



**Copyright:** © 2021 by the authors. Licensee MDPI, Basel, Switzerland. This article is an open access article distributed under the terms and conditions of the Creative Commons Attribution (CC BY) license (<https://creativecommons.org/licenses/by/4.0/>).

## 1. Introduction

Ceiling and visibility are two of the most important weather elements responsible for severe weather hazards for aviation. At least 29% of aviation accidents that occurred during the 2000–2011 period can be attributed to weather [1]. Based on data collected between 2009 and 2013 by the US Federal Aviation Agency (FAA), low ceiling and visibility conditions are responsible for over 27% of weather-related aviation accidents and 70% of fatalities [2]. Accuracy and calibration of instruments that measure visibility (VIS), cloud ceiling, relative humidity (RH), and temperature (T) are very important for accurate nowcasting and forecasting of visibility and cloud ceiling. These parameters also have critical importance for the validation of numerical weather prediction (NWP) and climate models. Based on a number of climate model simulations, on average, atmospheric absolute humidity is expected to increase in response to the increase in anthropogenic greenhouse

gases and the associated increase in temperature [3–5]. This is particularly true in the upper troposphere, where water vapor plays a significant role in the global radiation budget as a greenhouse gas [4]. Since RH is defined as the ratio of the amount of water vapor ( $q_v$ ) to the maximum amount expected at a given T when the atmosphere is saturated ( $q_s(T)$ ), the effect of increasing both  $q_v$  and  $q_s$  has a compensating effect on RH. As a result, the observed global change in surface RH during 1976–2004 was relatively small ( $\approx 0.6\%$ ) [6] and thus requires accurate measurements to be detected. At the surface level, RH is also used for visibility prediction applications (e.g., [7,8]).

Currently, standalone meteorological sensors are being used autonomously in some airports and remote locations. However, there have been limited studies of the accuracy of these instruments or how they compare with human observation. Data collected using the Vaisala FD12P sensor and human observation in southern Ontario [7] showed that, on average, human observers record higher VIS values by about 20% compared to measurements (VIS < 15 km) obtained using optical probes, with a mean difference (MD) of about 700 m. They also found that the Rotronic RH/T sensor underestimated the RH near the saturation point when compared with more standard instruments, such as the AES-Dewcell instrument that will be described in the following section.

The purpose of this study was to test, validate, and estimate uncertainties of a number of commonly used ground-based and remote-sensing instruments based on observations collected using well-established standard reference instruments and human-based observations. To achieve this, two years (2015–2016) of surface observation data, collected as part of the 4Wing Cold Lake Research project during 2015–2016 at Cold Lake, Alberta, was used. The remainder of the paper is organized as follows. In Section 2 the materials and methods are discussed, the results of the data analysis are given in Section 3, and the summary and conclusions are given in Section 4.

## 2. Materials and Methods

### 2.1. Study Area

The study area (Figure 1), the Cold Lake Regional Airport (CYOD), is located in northeastern Alberta, Canada (at 541 m MSL; 54 N, 110 W). In addition to the special ECCC observation site used in this study, there is a collocated permanent meteorological hourly observation (METAR) site used by the Canadian Department of National Defense (DND) within the CYOD airport, as indicated in the figure. The region is generally characterized by a humid continental climate with warm summers and cold winters [9,10]. To the west and northwest of the airport, there are four small lakes (Marie, Ethel, Crane, and Hilda), and to the northeast of the airport, two large lakes (Cold Lake and Primrose Lake) are known to contribute to the moistening of the atmosphere and affect the formation of precipitation and other weather phenomena when the flow is north-easterly. The west and southwest sides of the airport are surrounded by the Beaver River valley with an east–west orientation, which is also known to contribute various weather conditions including fog and lower ceilings and visibilities at the airport [9,10]. More discussions about the meteorological conditions of the location are given in Section 3.

### 2.2. Instruments and Data

The meteorological instruments used in this study are shown in Figure 1c. They include the Jenoptik CHM15k ceilometer, the Vaisala FS11P, and PWD22 present weather sensors, which measure VIS, precipitation intensity and type, and the radiometric, microwave radiometer (MWR) model MP-3000A, which measures cloud base height (CBH) and RH. The RH and T measured using the Vaisala WXT520 and AES-Dewcell sensors at the ECCC and DND site, respectively, were also used in the analysis (see Figure 1b). The complete descriptions of the instruments are given in [9,10]. Here, we will briefly discuss the instruments.

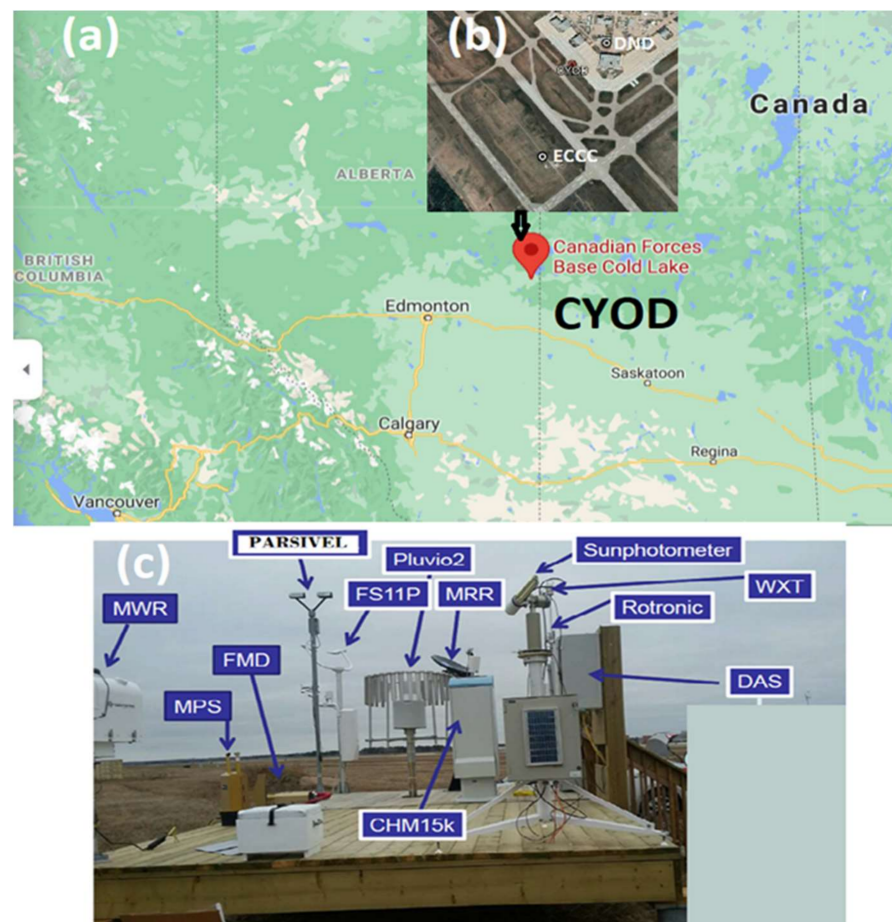


**Figure 1.** The geographical locations of CYOD (Canadian Air Force base) and the surrounding areas (a) and observation sites used in this study are marked as ECCC. A collocated meteorological terminal air report (METAR) observation site used by the DND is also shown (b) and the instruments set up at the ECCC site are shown in (c).

The MP-3000A MWR is equipped with one zenith infrared (9.6–11.5  $\mu\text{m}$ ) sensor that retrieves cloud base brightness temperatures from which the CBH can be determined. The radiometer also incorporates measurements of RH and T at the ground level, using the Rotronic RH/T sensor, into its atmospheric profiling algorithms [11]. The RH and T were also measured using another Rotronic HygroMet MP102 RH/T sensor. The HygroMet MP measures RH with a ROTRONIC Hygromer<sup>®</sup> IN1 capacitive sensor and T with a Pt100 resistance temperature detector (RTD). Based on the manufacturer's data sheet, the accuracy of these sensors at 23  $^{\circ}\text{C}$  is given as  $\pm 0.8\%$  and  $\pm 0.1$   $^{\circ}\text{C}$ .

The Vaisala WXT520 measures T and RH. The instrument is equipped with a capacitive ceramic THEMOCAP sensor for measuring air T and a capacitive thin film polymer HUMICAP180 sensor for RH measurements. According to the data given by the manufacturer, the accuracy of the WXT520 for measuring T is  $\pm 0.3$   $^{\circ}\text{C}$  (for  $-52$   $^{\circ}\text{C} < T < 60$   $^{\circ}\text{C}$ ), and the accuracy for measuring RH varies based on the measured RH ( $\pm 3$  for  $0 < \text{RH} < 90\%$ ) and  $\pm 5\%$  for  $90 < \text{RH} < 100\%$ ).

As discussed earlier, the RH and T were also measured at the DND site, which is approximately 948 m away from the ECCC site (see Figure 1b). The instrument used to measure RH and T at the DND site is the Atmospheric Environment Service (AES) Remote Temperature and Dewpoint Measuring Dewcell System Type 2, which is housed in a Stevenson screen. This is the standard instrument used operationally in Canada at weather stations, including those at major airports [12–14]. A Dewcell measures Td with a temperature sensor covered with a wick soaked in a solution of lithium chloride, which is

heated until its vapor pressure is in equilibrium with the ambient air. Using measurements of the  $T$  and  $T_d$ , the RH can be calculated. This sensor is designed to operate between  $-80\text{ }^{\circ}\text{C}$  and  $60\text{ }^{\circ}\text{C}$ . The accuracy of the Dewcell measuring  $T_d$  is close to  $\pm 0.5\text{ }^{\circ}\text{C}$  [15,16]. At colder temperatures ( $T_d < -10\text{ }^{\circ}\text{C}$ ), the accuracy is estimated to be lower ( $\pm 1.5\text{ }^{\circ}\text{C}$ ) [14]. The sensor is also checked for accuracy every week by comparing the reading to that of a reading taken from a psychrometer, which is also housed in a ventilated Stevenson screen. Acceptable accuracy with temperatures above  $0\text{ }^{\circ}\text{C}$  is up to  $\pm 1.0\text{ }^{\circ}\text{C}$  for both the temperature and the dewpoint, and for temperatures below  $0\text{ }^{\circ}\text{C}$ , accuracy is up to  $\pm 2.0\text{ }^{\circ}\text{C}$ . If the Dewcell is out of these tolerances, it must be taken out of service and properly cleaned and a minimum of three comparisons taken to ensure accuracy. Thus, the DND site Dewcell is a good instrument to calibrate and validate other sensors that are normally factory calibrated and not regularly checked for accuracy.

The Vaisala PWD22 and FS11P sensors measure precipitation, precipitation type, and visibility based on a forward light scattering principle with some minor difference in the scattering angle utilized. Both probes have similar configurations with two arms, one with a near-infrared transmitter and the other with a receiver. The two arms are aligned at certain angle so that the receiver can capture the scattered light if it is forward scattered at a given angle. In case of the PWD22, the angle is set at  $45^{\circ}$ ; for the FS11P, the angle is  $42^{\circ}$ . These instruments are also equipped with a heated capacitive surface that captures falling precipitation particles and evaporates them to obtain a liquid water equivalent measurement. The precipitation intensity and type are obtained by means of signal processing software that analyzes the voltage output from the receiver, along with the current temperature. Using a proprietary algorithm, the sensors calculate VIS using the measured extinction (Ext) ( $\text{VIS} = 3/\text{Ext}$ ) and an assumed threshold for visual contrast based on an equation derived under the assumption of scattering of light by a black object viewed under sunlight [7,17,18]. The Vaisala present weather sensors identify a number of precipitation types including fog, mist or haze, snow, ice crystal, rain, drizzle, and freezing rain. If no precipitation is detected, fog is identified when the 10 min averaged visibility is less than 1 km. When the 10 min averaged visibility is between 1 km and 10 km, mist, haze or smoke conditions are identified depending on the ambient relative humidity.

During nighttime, however, when done correctly, visibility must be calculated based on a different assumption involving how far away an undirected artificial light can be seen by the human eye [7,19], which is usually referred to as Allard's law [19]. Naturally, the human eye sees a light source at night from further away than a black object during the daytime under sunny conditions [7]. Most present weather probes, including the FS11P and PWD22, however, calculate VIS based on extinction alone during nighttime, since background light and light source intensity data are not readily available [7]; hence, there is some ambiguity in comparing measured and METAR-based visibilities. Furthermore, these instruments also have relatively small sample volumes and are therefore not so straightforward to compare against human-based observation without ambiguity, although longer time averaging can help to compensate for this problem.

The Jenoptik model CHM15k ceilometer transmits one ns laser pulses at a wavelength of 1064 nm with a 5–7 kHz pulse repetition frequency. The backscattered signal is detected with adjustable temporal and range resolutions, which are usually set to 30 s and 15 m for an acquisition of a single vertical profile. The backscattering profile from atmospheric targets is measured over the range of 30 m to 15 km, with full overlap height of about 100 m. Using the backscattered signal information, the ceilometer calculates three cloud base heights (CBHs), as well as aerosol layers, in the planetary boundary layer using proprietary software. In this paper, the CBHs representing the first (lowest) and the second cloud layers are designated as CBH1 and CBH2, respectively. Due to the small sampling area, ceilometer data is subject to not reporting clouds not directly overhead and over-reporting clouds that linger overhead, particularly spatially limited clouds such as convective clouds with moderate to great vertical development (personal communication, Maksim Houde, a weather observer at the airport). The CBH measurements can also be

affected by precipitation and hence, in this study, all precipitation cases (identified using the present weather sensors) were removed from the data.

### 2.3. Human Observation of Visibility and Ceiling

Human observations of VIS were made using designated visibility markers situated at different directions within a 360° view around the airdrome. These markers were viewed under sunlight during the daytime and with artificial light during the nighttime. Normally, the airdrome is divided into eight equal sectors and the prevailing VIS is determined based on the value estimated using the 5/8 portion of the airdrome and then reported in statute miles (SM) at increments of 1/8 SM, 1/4 SM, 1 SM, and 5 SM, depending on the observed visibility. For example, within the observed visibility range (3 SM < VIS < 15 SM), the prevailing VIS is reported at an increment of 1 SM (1.61 km), which is quite coarse as compared to the instruments that measure VIS in increments of 1 m. This type of reporting can be problematic in the presence of localized phenomena such as fog, which is normally reported in remarks by an observer. Therefore, it is not trivial to make definitive conclusions regarding the accuracy of the instruments for measuring VIS as compared to human observation.

According to the Manual of Surface Observation [20] in Canada, ceiling is defined as “the height above ground or water of the base of the lowest layer of cloud where the summation amount exceeds half the sky (more than 5/10 or 4/8); or the vertical visibility in a surface-based layer that completely obscures the whole sky”. Once the ceiling is identified, the height can be determined using a hand-held or permanently installed ceilometer. At Cold Lake, a permanently installed ceilometer is used. This combined method can eliminate some of the ambiguities associated with the human guessing and ceilometer limitations mentioned earlier.

The instruments mentioned above collected data at 1 min time intervals, and the METAR data that includes the AES RH/T sensor was reported on an hourly and sub-hourly basis. For this study, combined datasets were prepared for appropriate time intervals that matched the METAR data. Although there are some uncertainties associated with both human observation and instrument measurements, it is very important to test how the instruments compare with METAR data, since they are increasingly being used autonomously for aviation applications. To minimize the uncertainty in the ceiling height and VIS comparison against human observation, the comparisons were performed only when the observer identified a ceiling that could compensate for the instrument sampling area issues mentioned earlier. The combined hourly and sub-hourly (specials) data measured and reported from January–December during the 2015–2016 period were used in this study.

## 3. Results

### 3.1. Meteorological Conditions

#### 3.1.1. Winter

It is expected that the weather conditions at Cold Lake during winter leading to low visibility conditions are associated with both large-scale (synoptic) and small-scale (local) atmospheric flows. It has been reported that snow is the predominant precipitation type at Cold Lake [9,10], and hence the majority of the low visibilities were expected to be associated with falling and blowing snow, but, as will be shown later, a significant portion of the reduced visibilities observed were also related to fog.

Figure 2 shows meteorological conditions in November 2016. The data plotted in the figure includes VIS based on both METAR ( $VIS_{METAR}$ ) and the PWD22 sensor ( $VIS_{PWD22}$ ), RH based on METAR ( $RH_{AES-Dewcell}$ ), and the Rotronic humidity sensor ( $RH_{Rot}$ ) data (a). The precipitation intensity and type as determined by the PWD22, wind speed (WS) and wind direction (WD) measured using the WXR520 probe, and temperature (T) measured using the Rotronic sensor are also shown in b and c. It is interesting to note the significant variation in the observed temperature at Cold Lake in November, which ranges from  $-8\text{ }^{\circ}\text{C}$

to 16 °C (c); therefore, it is unlikely for the lake to be frozen under such conditions. The wind speed varied from 1 ms<sup>-1</sup> to near 7 ms<sup>-1</sup>. Closer scrutiny of the meteorological conditions during the reduced visibility events observed on 2, 20, and 23 November overnight, and on 24 November around 1 PM local time revealed that they were associated with snow. All other cases of reduced visibility events occurred overnight without precipitation during calm atmospheric condition (WS < 2.5 ms<sup>-1</sup>) with RH near saturation; thus, these events appeared to be related to radiative cooling (radiation fog). The exception is the one event on 24 November that occurred before midnight, which appeared to be related to advection associated with east and southeasterly flow with WS between 3 ms<sup>-1</sup> and 5 ms<sup>-1</sup>. The predominate wind directions during the light snow were north and northwesterly (c), suggesting that the lake may have some impact; however, during fog events, the predominant wind direction was southeasterly, suggesting some contributions of the local river valley. It is worth noting that the RH included in the METAR data (RH<sub>AES-Dewcell</sub>) was always higher than the RH<sub>rot</sub> near saturation; this will be discussed later in more detail. It can be seen also that some of the low visibility events (e.g., on 3, 14, and 17 November) reported by the present weather sensor were not reported by the human observer (a); this could be related to the fact that the human observer only reported prevailing visibility, as discussed earlier.

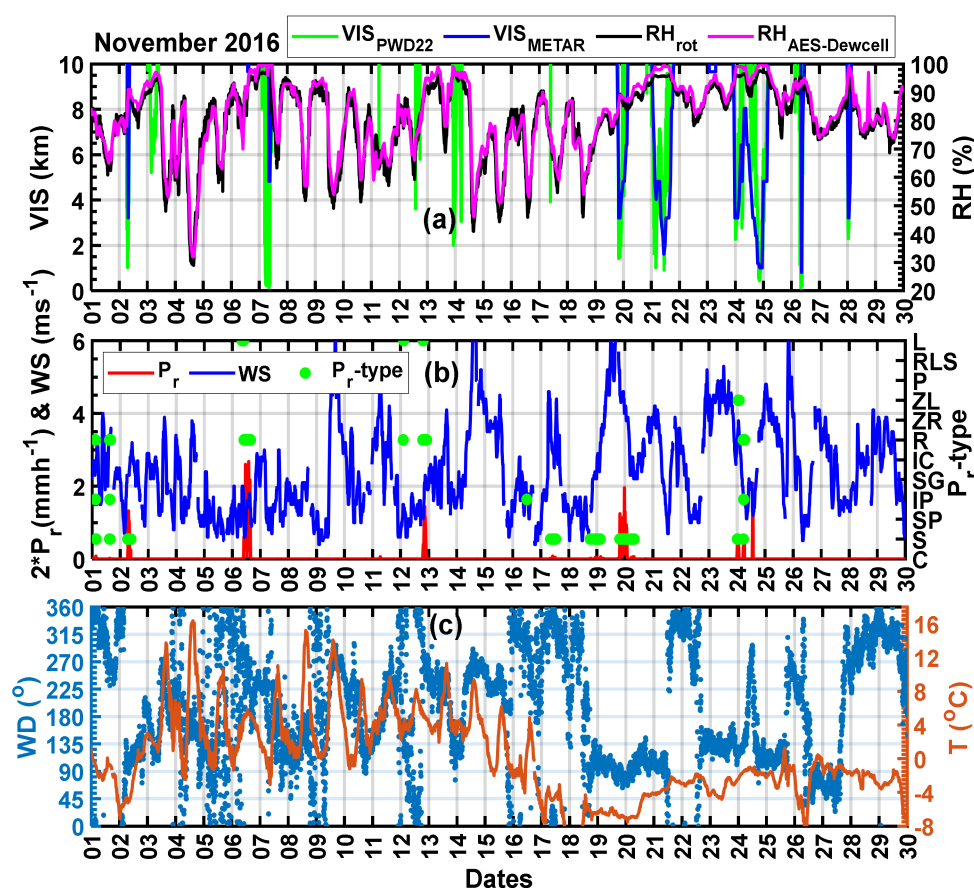


**Figure 2.** (a) The observed visibilities based on both PWD22 and METAR ( $VIS_{PWD22}$  and  $VIS_{METAR}$ ) and RH ( $RH_{METAR}$  and  $RH_{AES-Dewcell}$ ); (b) wind speed (WS), precipitation and type; (c) temperature (T) and wind direction. Precipitation type symbols (c = clear, SP = snow pellets, IP = ice pellets, SG = snow grain, IC = ice crystals, R = rain, ZR = freezing rain, ZL = freezing drizzle, P = unknown, RLS = rain + drizzle + snow, and L = drizzle).

The meteorological conditions for December 2016 are given in Figure 3. The first 3 days of December were relatively warm, near  $-5$  °C, but cooled after that, reaching  $-30$  °C on 17 December, and then warmed up to near zero in late December. The wind speed remained less than 8 ms<sup>-1</sup> for the entire month except on 19 December, when the WS reached 10 ms<sup>-1</sup>.

During the colder temperature period ( $T < -5\text{ }^{\circ}\text{C}$ ) (b), the RH did not exceed 90%, even during snow events. It is also interesting noting that  $\text{RH}_{\text{rot}}$  was smaller than  $\text{RH}_{\text{AES-Dewcell}}$ , particularly when precipitation was not reported. The temperature dependence of RH measurements is not discussed in this paper, but is worth exploring to better understand the observed differences. In December, the reduced visibilities were mainly related to light snow. The reduced visibility that occurred on 2 December appeared to be related to freezing fog, but the one that occurred on 9 December at very cold temperatures could be related to ice fog. The predominant wind directions were easterly and southeasterly, similar to the November case, but the snow events mainly occurred when the predominant wind direction was westerly and northwesterly; hence, it is possible that the lakes had less impact in these cases.

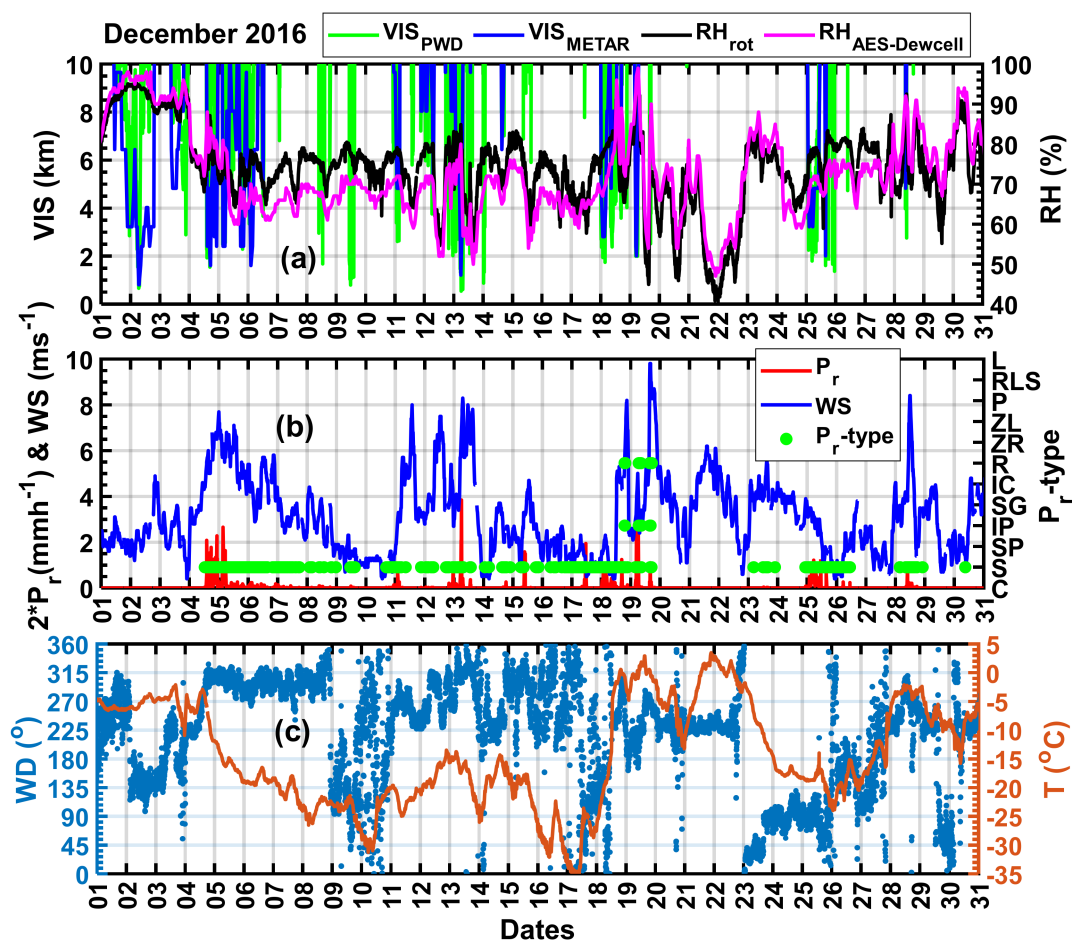


Figure 3. The same as Figure 2, but for the December case.

### 3.1.2. Summer

Figure 4 shows the meteorological conditions in June 2016. Panels (a) and (c) in the figure show that there is significant diurnal variability both in RH and T. The RH varied from 20% to 100% and T varied from  $5\text{ }^{\circ}\text{C}$  to  $30\text{ }^{\circ}\text{C}$ . The wind speed remained well below  $8\text{ ms}^{-1}$ . Based on a visual section of Panel a, the two humidity measurements generally agreed well ( $\text{RH}_{\text{rot}}$  and  $\text{RH}_{\text{AES-Dewcell}}$ ). Although the precipitation intensities were heavy at times, the visibility reduction due to rain events was weak compared to the fog and snow events. There were reports of shallow fog for 1 and 13 June and fog for 26 June by a human observer, and these low visibility events were well captured by the preset weather sensor (a).



attributed to the fact that the two sensors have slightly different scattering angles, but there may be also some connection to the way the manufacturers calibrated the instruments and the difference in the proprietary software used for processing the data. Vaisala does not reveal the algorithms used to calculate VIS in their user's manual.

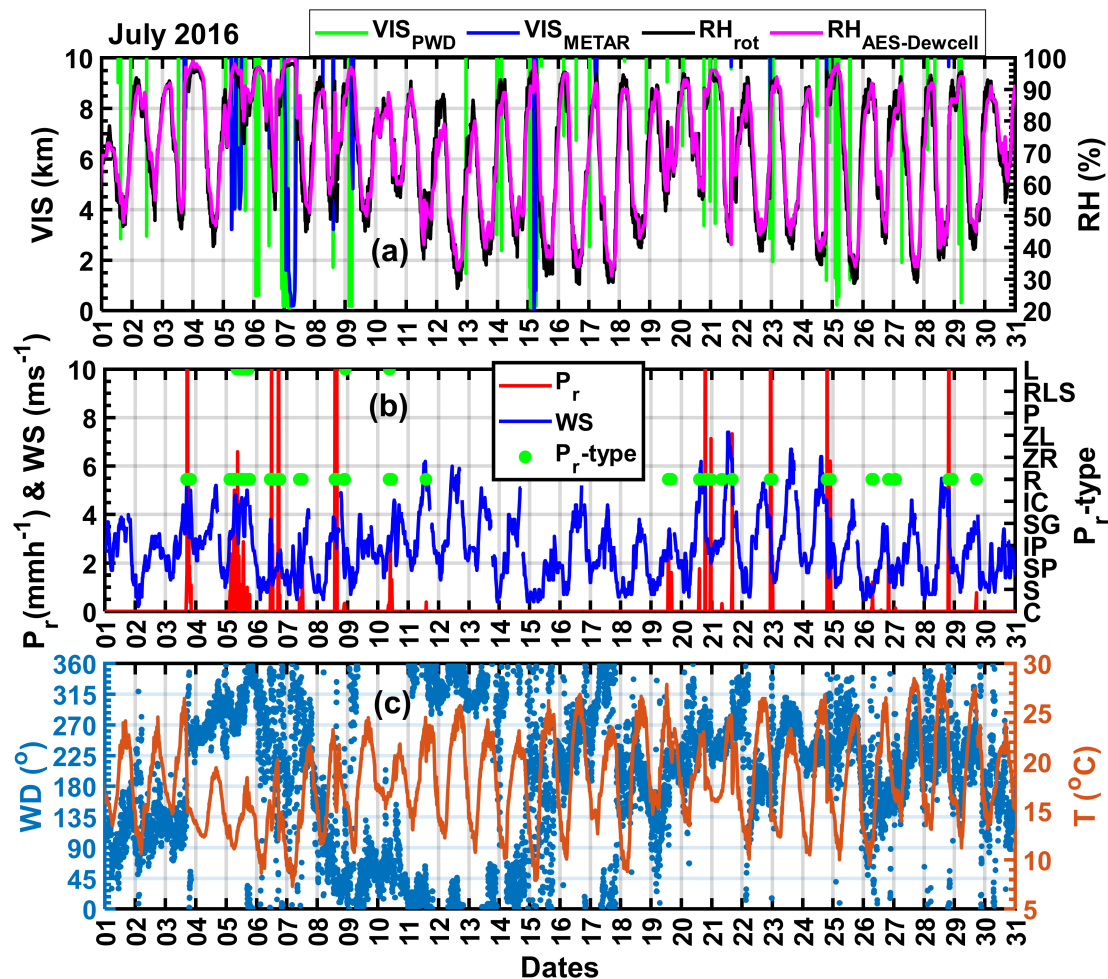


Figure 5. The same as Figure 4, but for the July case.

The extinction was derived following [7,17];  $3/\text{VIS}$  and snowfall rate ( $S_r$ ) data are given in Figure 6c for PWD22 and the data for FS11P is shown in Figure 6d. There is significant scatter between the observed extinction and the snowfall rate, as would be expected for such a high-resolution dataset. These scatterings are believed to be related to the difference in snow type and density [21]. Nonetheless, on average, the data showed good correlation ( $R \approx 0.7$ ) for both instruments. The power law relationships derived using the least-square fit method using the two data sets are given as

$$\text{Ext} = aS_r^b \quad (1)$$

where  $S_r$  is the snowfall rate in  $\text{mmh}^{-1}$ ,  $\text{Ext}$  is given in  $\text{km}^{-1}$ , and the coefficients  $a$  and  $b$  are 1.3 and 0.35, respectively, for the data collected using the PWD22 probe (c). The coefficients derived using the FS11P data were 1.34 and 0.36, respectively (d), in good agreement with the PWD22. However, as shown in Panels c and d, the extinction obtained using the new coefficients reported in this study significantly underestimated the extinction parameterization obtained based on data collected in southern Ontario [17]. This may be attributed to the difference in the snow type and density between the two

geographical locations, but more studies are necessary to better understand the reasoning behind these differences.

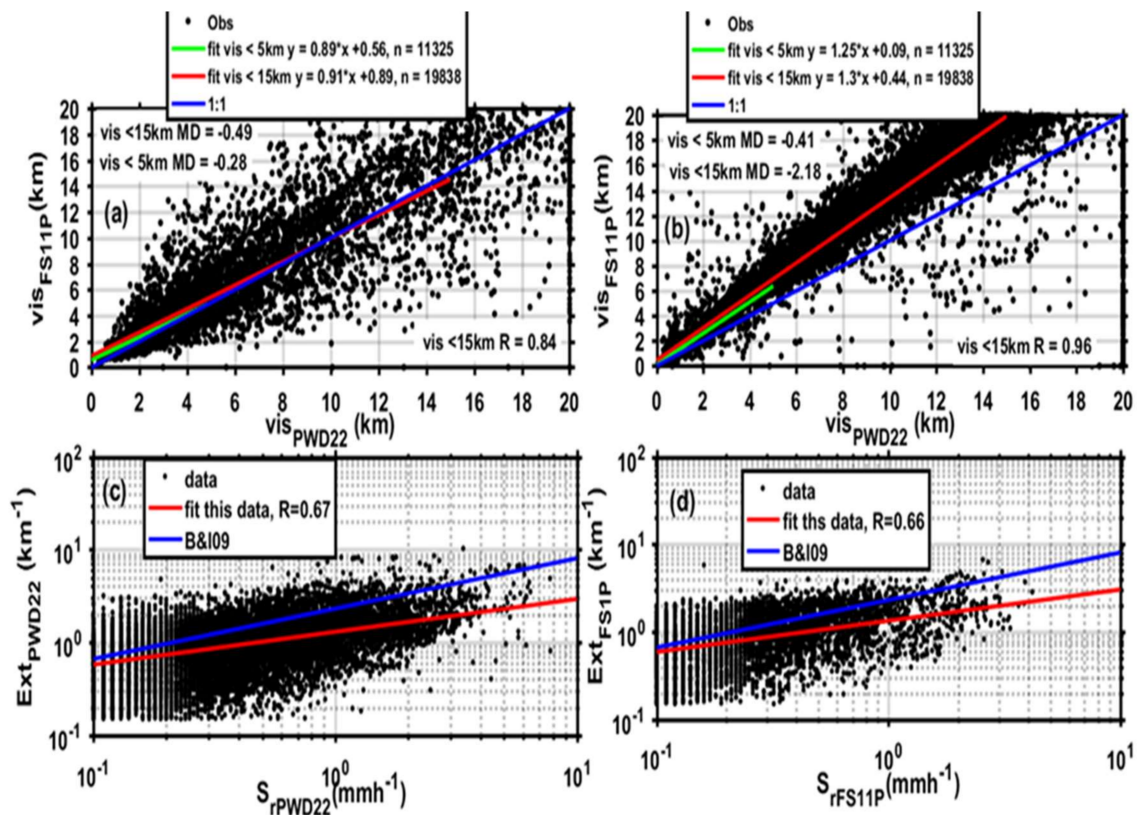


**Figure 6.** Visibility (VIS) comparison of FS11P and PWD22 during precipitation (a), during fog and clear conditions (b), the observed extinction ( $Ext = 3/\text{vis}$ ) and snowfall intensity ( $S_r$ ), and for FS11P (c). The data measured using the Vaisala FS11P (d) and PWD22,  $n$  represent the number of data points at 1 min intervals. The least square fits for this data are based on [17] (B&I09); the mean difference (MD) and the correlation coefficient (R) are also shown.

### 3.3. Visibility and Human Observation

Figure 7 shows the measured visibility using the Vaisala FS11P (a) and PWD22 (Panel b) plotted against human-based observation data ( $VIS_{\text{METAR}}$ ). When the data from these instruments are compared against the HO as indicated in (a) and (b), there is a significant quantization of the data, particularly at higher visibility values. This is mainly associated with the limited visibility markers normally used by the human observer for estimating VIS. The calculated correlation coefficient for both instruments for observed VIS < 10 km was better than 0.6, indicating an adequate agreement, but generally the human observer sees lower visibilities compared to the measurements, depending on the measured visibility. For visibilities lower than 4 km, which is normally considered the instrument flight rule (IFR) condition in aviation, the calculated MD between the HO and PWD22 data was about 0.98 km, which is slightly better than the FS11P (MD = 1.37 km). In even lower visibilities (less than 2 km), the MD between the HO data and the measurements was 640 m and 370 m for the FS11P and PWD22, respectively. The best-fit curves for visibilities less than 4 km and less than 10 km are also given in the figure.

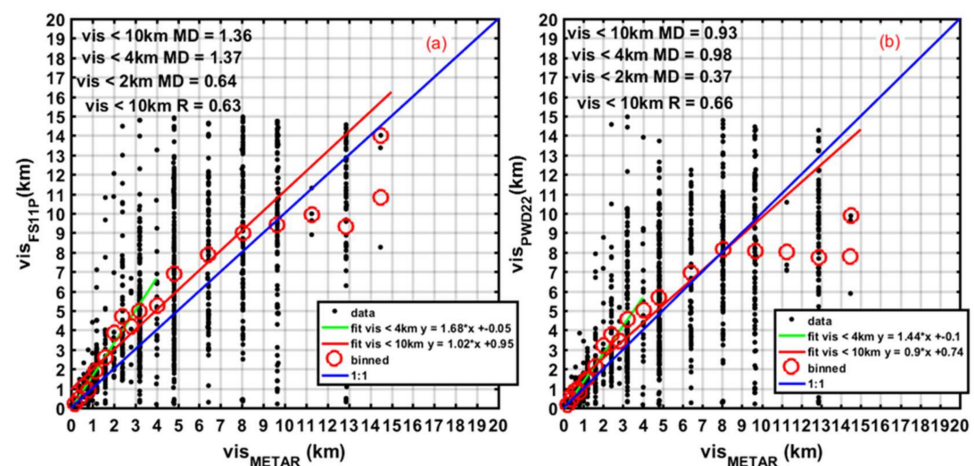


**Figure 7.** The measured visibility using the Vaisala FS11P (a) and PWD22 (b) plotted against human observer data ( $VIS_{METAR}$ ). The mean difference (MD) and the best fit lines for  $VIS < 4$  km and  $Vis < 10$  km.

Figure 7 shows the measured visibility using the Vaisala FS11P and PWD22. The METAR data shown in Figure 6 are segregated based on night and day conditions. The daytime data shows less quantization as compared to the nighttime data, but the correlation coefficient remained the same for the FS11. The PWD22 correlation significantly improved during daytime. On average, the FS11P measured larger visibilities as compared to the HO, particularly during the daytime. In contrast to the FS11P, the PWD22 probe measurements were close to the HO during the daytime. Based on these results, there is no indication that the visibility determined during the night by the HO is larger than the one measured by the instruments, as would be expected following Allard's law discussed earlier. This could be partly because not all of the visibility markers are individually equipped with their own lights, but rather viewed under nearby light sources.

Figure 8 shows the measured visibility using the Vaisala FS11P, PWD22 and METAR shown in Figure 7 segregated based on night and day time conditions. The daytime data shows less quantization as compared to the nighttime data, but the correlation coefficient remained the same for the FS11P, but the PWD22 correlation significantly improved during daytime. On average, the FS11P measured larger visibilities as compared to the HO particularly during the daytime. In contrast to the FS11P, the PWD22 probe measurements were close to the HO during the daytime. Based on these results, there is no indication that the visibility determined during the night by the HO is larger than the one measured by the instruments as would be expected following Allard's law discussed earlier. This could be partly because not all of the visibility markers are individually equipped with their own lights but rather viewed under nearby light sources.

### 3.4. Cloud Base Height Measurement Comparisons

Figure 9 shows comparisons of the CBHs measured using the CHM15k (CBH1 and CBH2), MWR (CBH<sub>MWR</sub>), and HO (CBH<sub>METAR</sub>). The human observer, on average, reported higher CBH as compared to the ceilometer observation (a); the calculated MD for CBH < 10 km was 390 m and for CBH < 4 km, it was 100 m, which is much better for lower ceilings, and the correlation coefficient for all the data was near 0.80, which is strong (a). Similar to visibility, some quantization is obvious, particularly for CBH > 3 km. This could be attributed to the difference between the methods employed to estimate the CBH. The CBH determined using the MWR are larger for smaller CBH (< 2 km) and smaller for larger CBH when compared to both human observation and ceilometer data ((b) and (c)). The MD between CHM and MWR was ~1 km for both CBH < 4 km and CBH < 10 km (b). The MWR also exhibited similar behavior, as shown in (b) when compared against human observation (c), with a similar correlation of 0.65. The best-fit lines of the binned

data are also given. These results suggest that the CBH determined using the method adopted in the MWR should be used cautiously, particularly for lower cloud base heights. No significant correlation between the CBH<sub>2</sub> and CBH<sub>MWR</sub> was found (d).

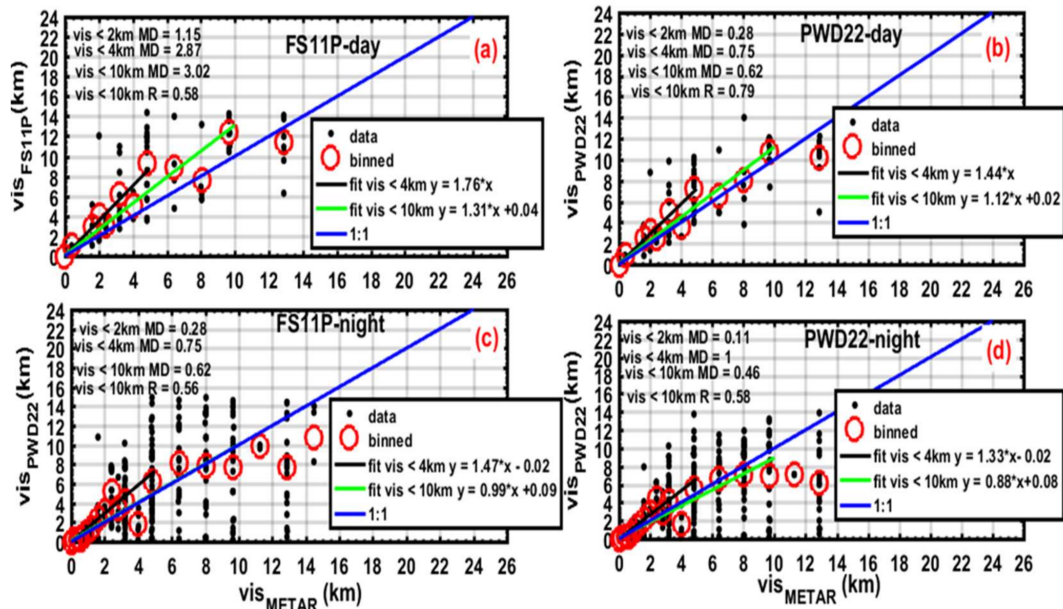


Figure 8. The measured visibility using the Vaisala FS11P (day (a) and night (c)) and PWD22 (day (b) and night (d)) plotted against human observer data ( $VIS_{METAR}$ ).

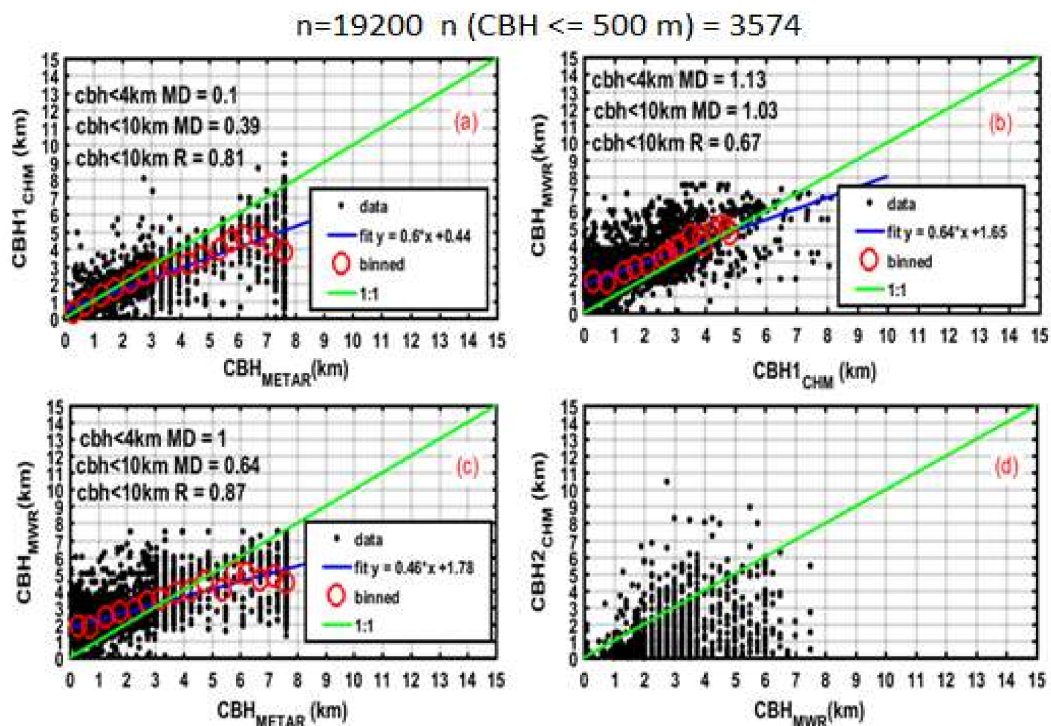
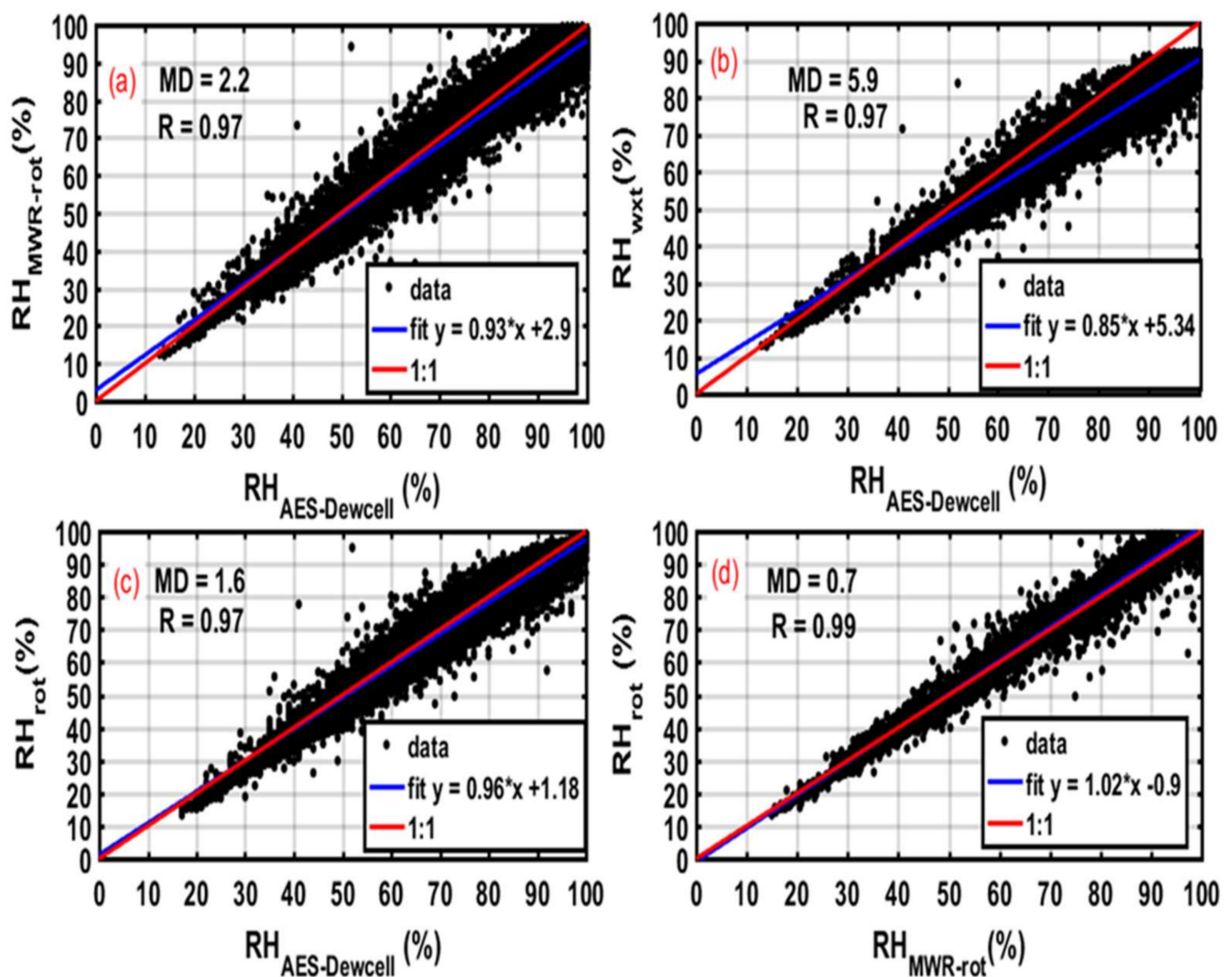


Figure 9. The lowest cloud base height (CBH1) measured using the CHM15 ceilometer ( $CBH1_{CHM}$ ) and MWR ( $CBH_{MWR}$ ) plotted against human observation ( $CBH_{METAR}$ ) ((a,c)), the  $CBH_{MWR}$  data plotted against the  $CBH1_{CHM}$  data (b), and the second cloud-base height ( $CBH2_{CHM}$ ) plotted against the  $CBH_{MWR}$  data (Panel d). The number of matched points ( $n$ ) and the number of points for  $CBH \leq 500$  m are also shown.

### 3.5. Relative Humidity and Temperature Measurements Comparisons

Figure 10 show the relative humidity measured using the Rotronic sensor used in the MWR ( $RH_{MWR}$ ) (a), the WXT520 ( $RH_{wxt}$ ) (b), and a second Rotronic sensors ( $RH_{rot}$ ) (c), plotted against the AES-Dewcell sensor (d) and the comparison of the two Rotronic sensors, ( $RH_{rot}$ ) and  $RH_{MWR-rot}$  (d). All the instruments correlated well ( $R = 0.97$ ) with the AES sensor, but underestimated the RH relative to the AES sensor, with a mean difference (MD) of 2% for the Rotronic sensors and 6% for the WXT sensor. The linear best-fit curves (also shown in the figure) showed that the bias increases with increasing RH. For example, when the true value is set at  $RH = 100\%$ , the measured values for  $RH_{MWR}$ ,  $RH_{rot}$ , and  $RH_{wxt}$  would be approximately 95.9%, 97.2%, and 90.34%, respectively, which corresponds to a 4%, 3%, and 9.5% underestimation, respectively, reflecting large uncertainty compared to the accuracy needed to detect the change in RH associated with anticipated climate change. The observed temperature comparisons similar to Figure 10 are shown in Figure 11. All the instruments agreed reasonably well, with a correlation coefficient ( $R$ ) better than 0.99 and a mean difference of less than  $0.1\text{ }^{\circ}\text{C}$ . The best fit and one-to-one curves are also shown and indicate good agreement between the instruments.



**Figure 10.** The relative humidity measured using the Rotronic sensor using in the MWR ( $RH_{MWR}$ ) (a), the WXT520 ( $RH_{wxt}$ ) (b), and a second Rotronic sensor ( $RH_{rot}$ ) (c), plotted against the AES-Dewcell sensor (d), and the comparison of the two Rotronic sensors ( $RH_{rot}$  and  $RH_{MWR-rot}$ ) (d).

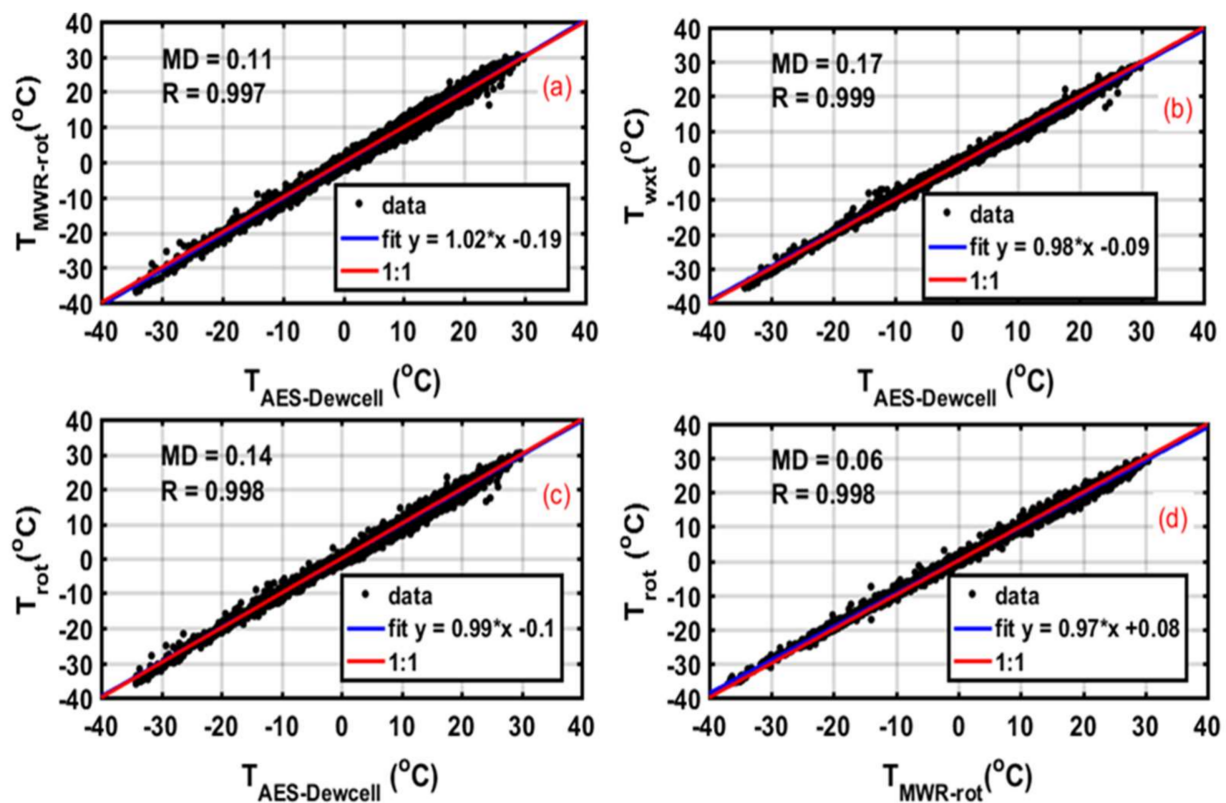


Figure 11. Similar to Figure 10, but for temperature in this case.

#### 4. Summary and Conclusions

Observations that were obtained using a number of commonly used ground-based in situ and remote-sensing instruments were tested against observations collected using well-established standard instruments and human-based observations. For this purpose, two years of surface observation data collected at Cold Lake, Alberta during the 2015–2016 time period was used. The specialized instruments that were tested include the Vaisala FS11P and PWD22 present weather sensors that measure horizontal visibility, the radiometric microwave radiometer (MWR) and Jenoptik CHM15k ceilometer that measure cloud base height, and the Rotronic, Vaisala WXT520, and AES-Dewcell that measure humidity (RH) and temperature (T). The main findings are given below:

Comparison of visibility measured using the Vaisala FS11P and PWD22 showed that although they are well correlated, the data exhibited significant scatter. The calculated mean difference (MD) varied from 280 m for visibility < 5 km to 490 m for visibility < 15 km under precipitation conditions, showing better agreement at lower visibilities. Generally, the FS11P measured larger visibilities compared to the PWD22. Under fog or clear conditions, the correlation between the two probes was better ( $R = 0.96$ ), but the FS11P measured higher visibilities as compared to the PWD22, with a MD of 410 m and 2180 m for visibilities < 5 km and < 15 km, respectively, indicating more discrepancy between the probes under fog or clear conditions than precipitation. This analysis shows the difficulty in measuring visibility and the determination of associated uncertainties.

When the visibilities measured using the FS11P and PWD22 were compared against human-based observation, the data showed significant quantization, particularly at higher visibility values. This is mainly associated with limited visibility markers used by the human observer for estimating visibility. The calculated correlation coefficient for both instruments with visibility < 10 km was better than 0.6, indicating good agreement, but generally the human observer reported lower visibility values. For visibilities less than 2 km, the human observer sees on average lower visibilities, with a MD of 640 m and 370 m as compared to the FS11P and PWD22, respectively. However, for visibilities lower

than 5 km, the calculated MD for the PWD22 was 0.98 km, which is better than the FS11P with a MD of almost 1.37 km, so the PWD22 probe appears to be slightly closer to human observation than the FS11P probe.

When the data was segregated based on night and day, the daytime data showed less quantization. On average, the FS11P measured higher visibilities as compared to human observation, particularly during the daytime. In contrast, the PWD22 probe measurements were close to human observation during the daytime.

Two visibility/extinction parameterizations as a function of snowfall rate were developed based on both FS11P and PWD22 measurements and the results were found to be similar, but the extinction obtained using the new coefficients reported in this study significantly underestimated the extinction parameterization obtained based on data collected in southern Ontario.

The CHM15 ceilometer on average measured lower cloud base height (CBH) compared to human observation and the calculated MDs were 390 m for CBH < 10 km and 100 m for CBH < 4 km. The correlation coefficient for the entire dataset was near 0.8, which is respectable.

The CBHs were over-estimated by the MWR for CBHs (<2 km) and under-estimated for higher CBHs. The MD between CHM15k and MWR was  $\approx 1$  km for both CBH < 4 km and CBH < 10 km, with no significant change. The CBH determined using the MWR also exhibited similar behavior when compared against human-based observations, with a relatively lower correlation of 0.65. These results suggest that CBH height determined using the method adopted in the MWR is not reliable, particularly for lower cloud base heights.

All the humidity sensors correlated well ( $R = 0.97$ ) with the AES-Dewcell sensor, but all underestimated the RH, with MDs ranging from 2% for the Rotronic sensors to 6% for the WXT sensor. The uncertainty became more significant at near saturation; for example for WXT520, the error was as much as 10% at 100% RH.

In contrast to the RH measurements, all the temperature sensors agreed quite well with a correlation coefficient ( $R$ ) better than 0.99, and with an MD of less than 0.1 °C.

Based on the findings in this study, treating the data measured using the stand-alone automated meteorological instruments similar to the data obtained by human observations is potentially misleading, as it requires some corrections and adjustments before being used for model validation, aviation weather, or other applications. As shown in this study, two similar instruments do not measure precisely the same visibility, illustrating the difficulty measuring this field. The same can be said even for measuring RH, particularly close to saturation. These discrepancies could be associated with the sensitivity of a give instrument, calibration, and other factors pertaining to the location and type of weather under which the instrument is being used.

**Author Contributions:** Project administration, funding acquisition, conceptualization, methodology, validation, formal analysis, data curation, writing—original draft preparation, F.S.B.; writing—review and editing, I.G. and J.A.M. All authors have read and agreed to the published version of the manuscript.

**Funding:** This research was partially funded by the National Search and Rescue New Initiative Fund (SAR-NIF) under the SAR project # SN201532.

**Institutional Review Board Statement:** Not applicable.

**Informed Consent Statement:** Not applicable.

**Data Availability Statement:** The data sets used in this study are not publicly available as yet, but can be requested from F.S.B.

**Acknowledgments:** We like to thank Mike Harwood and Robert Reed for helping with installation of the instruments at Cold Lake, and Robert Crawford for archiving the data. We also would like to extend our thanks to Jeff Baker, Maksim Houde, Amy Slade-Campbell, and Gordon Lee of DND for providing METAR data, and also Randy Blackwell for helping during the instrument installation process.

**Conflicts of Interest:** The authors declare no conflict of interest.

## References

1. Gultepe, I.; Sharman, R.; Williams, P.D.; Zhou, B.; Ellrod, G.; Minnis, P.; Trier, S.; Griffin, S.; Yum, S.S.; Gharabaghi, B.; et al. A Review of High Impact Weather for Aviation Meteorology. *Pure Appl. Geophys.* **2019**, *176*, 1869–1921. [[CrossRef](#)]
2. Fultz, A.J.; Ashley, W.S. Fatal weather-related general aviation accidents in the United States. *Phys. Geogr.* **2016**, *37*, 291–312. [[CrossRef](#)]
3. Held, I.; Soden, B. Water Vapor Feedback and Global Warming. *Annu. Rev. Energy Environ.* **2000**, *25*, 441. [[CrossRef](#)]
4. Soden, B.J.; Jackson, D.L.; Ramaswamy, V.; Schwarzkopf, M.D.; Huang, X. The Radiative signature of upper tropospheric moistening. *Science* **2005**, *310*, 841–844. [[CrossRef](#)] [[PubMed](#)]
5. Soden, B.J.; Wetherald, R.T.; Stenchikov, G.L.; Robock, A. Global cooling after the eruption of Mount Pinatubo: A test of climate feedback by water vapor. *Science* **2002**, *296*, 727–730. [[CrossRef](#)] [[PubMed](#)]
6. Dai, A.G. Recent Climatology, Variability, and Trends in Global Surface Humidity. *J. Clim.* **2006**, *19*, 3589–3606. [[CrossRef](#)]
7. Boudala, F.S.; Isaac, G.A.; Crawford, R.; Reid, J. Parameterization of runway visual range as a function of visibility: Application in numerical weather prediction models. *J. Atmos. Oceanic Technol.* **2012**, *29*, 177–191. [[CrossRef](#)]
8. Gultepe, I.; Isaac, G.A.; Joe, P.; Kucera, P.A.; Theriault, J.M.; Fisco, T. Roundhouse (RND) Mountain Top Research Site: Measurements and Uncertainties for Winter Alpine Weather Conditions. *Pure Appl. Geophys.* **2014**, *171*, 59–85. [[CrossRef](#)]
9. Boudala, F.S.; Isaac, G.A.; Filman, P.; Crawford, R.; Hudak, D. Performance of Emerging Technologies for Measuring Solid and Liquid Precipitation in Cold Climate as Compared to the Traditional Manual Gauges. *J. Atmos. Oceanic Technol.* **2017**, *34*, 167–184. [[CrossRef](#)]
10. Boudala, F.; Isaac, G.A.; Wu, D. Aircraft Icing Study Using Integrated Observations and Model Data. *Weather Forecast.* **2019**, *34*, 485–506. [[CrossRef](#)]
11. Ware, R.; Carpenter, R.; Güldner, J.; Liljegen, J.; Nehr Korn, T.; Solheim, F.; Vandenberghe, F. A multi-channel radiometric profiler of temperature, humidity and cloud liquid. *Radio Sci.* **2003**, *38*, 8032. [[CrossRef](#)]
12. Van Wijngaarden, W.A.; Vincent, L.A. Examination of discontinuities in hourly surface relative humidity in Canada during 1953–2003. *J. Geophys. Res.* **2005**, *110*, D22102. [[CrossRef](#)]
13. Vincent, L.A.; van Wijngaarden, W.A.; Hopkinson, R. Surface Temperature and Humidity Trends in Canada for 1953–2005. *J. Clim.* **2007**, *20*, 5100–5113. [[CrossRef](#)]
14. Déry, S.J.; Stieglitz, M. A Note on Surface Humidity Measurements In The Cold Canadian Environment. *Boundary-Layer Meteorol.* **2002**, *102*, 491–497. [[CrossRef](#)]
15. Brock, F.V. (Ed.) *Instructor's Handbook on Meteorological Instrumentation*; Note NCAR/TN-2371A, NCAR; NCAR Tech.: Boulder, CO, USA, 1984; p. 339.
16. Brock, F.V.; Richardson, S.J. *Meteorological Measurement Systems*; Oxford University Press: Oxford, UK, 2001; p. 290.
17. Boudala, F.S.; Isaac, G.A. Parameterization of visibility in snow: Application in numerical weather prediction models. *J. Geophys. Res.* **2009**, *114*, D19202. [[CrossRef](#)]
18. Koschmieder, H. The 'orie der horizontalen Sichtweite. *Beitr. Freien Atmos.* **1924**, *12*, 171–181.
19. Allard, E. *Me 'Morie sur l'Intensite ' et la Portee ' des Phares*; Dunod: Malakoff, France, 1876; p. 70.
20. Manual of Surface Weather Observations (MANOBS), 2015. Available online: [https://www.canada.ca/content/dam/eccc/migration/main/manobs/73bc3152-e142-4aee-ac7d-cf30daff9f70/manobs\\_7e-a19\\_eng\\_web.pdf](https://www.canada.ca/content/dam/eccc/migration/main/manobs/73bc3152-e142-4aee-ac7d-cf30daff9f70/manobs_7e-a19_eng_web.pdf) (accessed on 12 December 2021).
21. Rasmussen, M.R.; Vivekanadan, J.; Cole, J.; Myers, B.; Maters, C. Estimation of snowfall using visibility. *J. Appl. Meteorol.* **1999**, *38*, 1542–1563. [[CrossRef](#)]